Journal of Materials Chemistry C

ROYAL SOCIETY OF CHEMISTRY

PAPER

View Article Online
View Journal | View Issue

Check for updates

Cite this: J. Mater. Chem. C, 2026, 14, 5384

A next-generation fluorescent chemosensor for dual-mode detection of aluminium ions and DCP: a bridge between sensing and bio-imaging

Saurabh Gupta,†[a] Abhishek Kaundal,†[b] Gulshan Kumar,[c] Vijay Luxami *[b] and Kamaldeep Paul *[ab]

In the present work, we have rationally designed and synthesized a bis-naphthalimide-based "turn-on" fluorescent chemosensor, **BINNA**, capable of dual-analyte recognition with high sensitivity and selectivity for aluminium ions (Al^{3+}) and the nerve agent mimic diethyl chlorophosphate (DCP) in methanol medium. Distinct photophysical responses are observed: the addition of DCP induces a strong emission band at 370 nm, whereas the addition of Al^{3+} ions displays an intense emission band at 450 nm, allowing for clear spectral discrimination. The probe demonstrates outstanding detection capabilities, with detection limits reaching as low as 8.5 nM for DCP and 18.2 nM for Al^{3+}. High-resolution mass spectrometry (HRMS) analyses provide mechanistic insights into the interaction pathways of **BINNA** with each target analyte. Complementary theoretical investigations using computational modelling further corroborate the experimental findings. Beyond its role in solution-phase sensing, **BINNA**'s photonic properties are employed to construct a molecular logic gate system based on fluorescence signal outputs. The practical applicability of the sensor is validated through the successful detection of DCP and Al^{3+} in soil samples. Moreover, **BINNA**'s ability to visualize cellular uptake and fluorescence in live bacterial cells underscores its potential as a multifunctional probe for environmental analysis and advanced bio-imaging applications.

Received 29th December 2025,
Accepted 18th January 2026

DOI: 10.1039/d5tc04533a

rsc.li/materials-c

Open Access Article. Published on 19 January 2026. Downloaded on 5/10/2026 5:39:47 PM.
This article is licensed under a Creative Commons Attribution 3.0 Unported Licence.

1. Introduction

Chemosensors have emerged as pivotal tools in modern science, offering innovative solutions for environmental sustainability, health monitoring, and food quality control.[1] Their ability to provide rapid, cost-effective, and selective detection of various analytes has revolutionized traditional sensing methodologies.[2] Traditional detection methods like atomic absorption spectroscopy (AAS),[3] voltammetry,[4] and inductively coupled plasma mass spectrometry (ICP-MS)[5] have been instrumental in analytical chemistry. However, these techniques often require sophisticated instrumentation, are time-consuming, and lack the desired sensitivity and selectivity.[6,7] In contrast, chemosensors, especially those based on fluorophores, offer simplicity in synthesis, cost-effectiveness, and rapid detection capabilities.[8–10] Their detection limits, selectivity, and recoverability make them ideal for detecting various metal and biological ions.[11–13] Among the fluorophores, naphthalimide has garnered significant attention due to its unique properties: a flat aromatic ring system, π-electron deficiency, strong absorption in the visible region, high fluorescence quantum yield, significant Stokes shift, outstanding photostability, rapid response, high sensitivity and selectivity, and ease of structural modification. These characteristics make naphthalimide an excellent candidate for developing chemosensors.[14–18]

Aluminium ions (Al^{3+}) are prevalent in daily life, found in cooking vessels, the paper industry, textiles, agriculture, and food additives.[19] Although Al^{3+} is non-essential for humans, elevated concentrations can lead to severe health issues, including Parkinson's disease, Alzheimer's disease, osteomalacia, and central nervous system malfunctions.[20,21] The World Health Organization (WHO) recommends a permissible limit of 7.14 μM in water and 3–10 mg per day for human intake.[22] Currently, most of the Al^{3+} detecting sensors face challenges due to interference from other metal ions like Hg^{2+}, Cu^{2+}, Zn^{2+}, and Fe^{3+}. Therefore, there is an urgent need to develop novel chemosensors that can selectively detect Al^{3+} ions without interference.[23,24] Recent studies have shown that naphthalimide-based chemosensors exhibit high selectivity and

[a] TIET-VT, Centre of Excellence in Emerging Materials, Thapar Institute of Engineering and Technology, Patiala, Punjab, 147004, India
[b] Department of Chemistry and Biochemistry, Thapar Institute of Engineering and Technology, Patiala, 147001, India. E-mail: vluxami@thapar.edu, kpaul@thapar.edu
[c] Department of Chemistry, Banasthali University, Banasthali, Newai, 304022, Rajasthan, India
† Contributed equally.

This journal is © The Royal Society of Chemistry 2026

Open Access Article. Published on 19 January 2026. Downloaded on 5/10/2026 5:39:47 PM. This article is licensed under a Creative Commons Attribution 3.0 Unported Licence.

sensitivity for Al^{3+} detection, making them promising candidates for practical applications.[25,26]

Moreover, organophosphorus compounds (OPs), including diethyl chlorophosphate (DCP), are highly toxic substances used as pesticides, herbicides, and chemical warfare agents.[27] These compounds inhibit acetylcholine esterase (AchE), leading to the accumulation of acetylcholine, which disrupts nerve function and causes respiratory failure and death.[28] DCP is often used as a simulant for G-series nerve agents like soman (GD), sarin (GB), and tabun (GA) due to its similar structure and reactivity.[29,30] Given the high toxicity of OPs, researchers have focused on developing chemosensors for their detection.[31] Recent advancements have led to the development of chemosensors capable of detecting DCP with high sensitivity and selectivity, offering potential for real-time monitoring and rapid response in case of exposure.[32] Therefore, the development of chemosensors, particularly those based on fluorophores like naphthalimide, offers a promising avenue for the selective and sensitive detection of harmful ions and nerve agents. These advancements not only enhance the ability to monitor environmental and biological systems but also contribute significantly to public health and safety.

1.1. Design of BINNA and novelty of the work

In recent years, a variety of chemosensors have been designed and synthesized for the detection of Al^{3+} ions and DCP.[33–35] These chemosensors can detect either Al^{3+} or DCP, with detection limits ranging from 23 μM to 98 nM (Table S1). These chemosensors are generally Schiff bases incorporated into some fluorophores such as naphthalimide, rhodamine, phenanthroimidazole, *etc.*, but none of the developed chemosensors has the ability to detect Al^{3+} and DCP simultaneously, thereby increasing the synthesis cost of developing different chemosensors for both analytes and decreasing their multifunctional applications in biological detection and environmental monitoring. Thus, there is a need for the development of new chemosensors that can simultaneously detect both analytes and have better detection limits (Fig. 1). Recently, Zhang *et al.*[25] reported a naphthalimide-based chemosensor containing a Schiff base unit formed from (*N*,*N*-diethylamino)benzaldehyde, while an alkyl group (ethyl morpholine) was introduced at the anhydride position of naphthalimide. The reported sensor detected the Al^{3+} ions in MeOH with a limit of detection in the micromolar range. Similarly, in 2023, Jain *et al.*[26] developed a naphthalimide-based chemosensor appended with a Schiff base unit derived from (*N*,*N*-diethylamino)salicylaldehyde. They have used butylamine as an alkyl group at the anhydride position of naphthalimide; their developed sensor detects DCP in CH_3CN with a detection limit in the micromolar range. Over the past few years, naphthalimide with a Schiff base unit has been largely explored for its sensing ability, but up to now, no report on a bis-naphthalimide moiety bearing Schiff base units has been published. In this context, we have developed a novel chemosensor (**BINNA**) by modifying a previously reported naphthalimide-based probe, specifically replacing the alkyl chain with an additional naphthalimide unit and substituting (*N*,*N*-diethylamino)salicylaldehyde with naphthaldehyde to create a bis-naphthalimide architecture. Our developed chemosensor sequentially detects both the metal ion, *i.e.* Al^{3+}, and the nerve agent DCP in methanol, which could effectively reduce the synthesis cost of different chemosensors. The probe **BINNA** exhibits better selectivity and sensitivity than the reported chemosensors with a limit of detection in the nanomolar range for both analytes. Moreover, **BINNA** also exhibited aggregation effects, which were supported by DLS and SEM studies. Initially, **BINNA** is non-fluorescent, but upon interacting with Al^{3+} or DCP, an enhancement in the fluorescence intensity of the probe is observed, thus building a "turn-on" fluorescent probe for detecting metal ions and nerve agents. This capability not only improves sensitivity but also offers a dependable fluorescence-based approach for the selective detection of Al^{3+} ions and DCP. The probe also demonstrates strong performance in identifying both analytes in live bacterial cells, highlighting its versatility and effectiveness for practical and real-world applications.

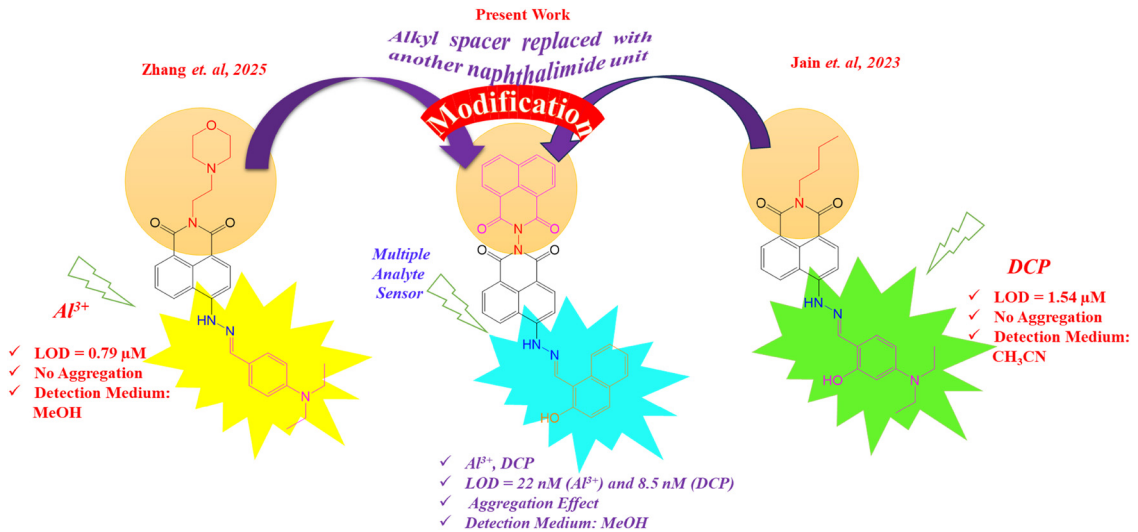

Fig. 1 Design of the probe **BINNA**.

Open Access Article. Published on 19 January 2026. Downloaded on 5/10/2026 5:39:47 PM. This article is licensed under a Creative Commons Attribution 3.0 Unported Licence.

2. Experimental section

2.1. Materials and characterisation

The chemicals used for the synthesis of **BINNA** were purchased from various suppliers, including Sigma-Aldrich Ltd, Loba Chemie, and Spectrochem, depending on their availability. All solvents utilized in the synthesis were of spectroscopic grade and procured from Spectrochem. Reaction progress was monitored using thin-layer chromatography (TLC) on silica plates coated with silica gel GF-254, obtained from Spectrochem Pvt Ltd, India. UV light at wavelengths of 254 or 365 nm was employed to visualize changes on the TLC plates. Compound purification was carried out using column chromatography with silica gel (60–120 mesh). ^{1}H and ^{13}C NMR spectra were recorded at room temperature using a BRUKER ECS-400 MHz spectrometer (400 MHz for ^{1}H and 100 MHz for ^{13}C). NMR samples were prepared in deuterated DMSO (DMSO-d_6) using tetramethylsilane (TMS) as the internal standard, with chemical shifts reported in parts per million (ppm). High-resolution mass spectrometry (HRMS) data were obtained using a XEVO G2-XS QTOF spectrometer.

2.2. Computational methods

Geometry optimization of the probe **BINNA** in its ground state (S_0) was performed using the B3LYP functional with the 6-31G(d) basis set as implemented in Gaussian 16. To account for experimental conditions, the solvation effect of methanol was incorporated using the integral equation formalism polarizable continuum model (IEFPCM). The absence of imaginary vibrational frequencies confirmed the stability of the optimized molecular structures. Excitation energies were calculated employing time-dependent density functional theory (TD-DFT). Given the molecular flexibility of **BINNA** at –C═N– and –N–N– linkages, multiple conformers were explored at the S_0 state. Two stable conformers, designated **BINNA**-C1 and **BINNA**-C2, were identified with relative energies of 0.00 and 2.57 kcal mol^{-1}, respectively. Boltzmann population analysis at 298 K indicated distributions of 98% for **BINNA**-C1 and 2% for **BINNA**-C2, leading to the selection of **BINNA**-C1 for subsequent analysis (Fig. S1). Further geometry optimizations and TD-DFT calculations were carried out using various exchange–correlation functionals (CAM-B3LYP, B3PW91, PBE0, and M06-2X) and basis sets (6-31G(d), 6-311G(d) and 6-311G(d,p)). The CAM-B3LYP/6-31G(d) level of theory yielded results in the closest agreement with experimental data and was therefore employed for a detailed discussion of the electronic and optical properties. Molecular electrostatic potential (MEP) mapping was also conducted to assess charge distribution across the molecule.

2.3 Synthesis of BINNA

2.3.1. Synthesis of the compound BIN-Br (1). A stirred solution of 2-amino-1*H*-benzo[*de*]isoquinoline-1,3(2*H*)-dione (500 mg, 2.3 mmol) in 50 mL of ethanol was treated with 6-bromo-1*H*,3*H*-benzo[*de*]isochromene-1,3-dione (780 mg, 2.8 mmol) along with a catalytic amount of zinc acetate. The reaction progress was continuously monitored by thin-layer chromatography, and the reaction was refluxed until the starting material was completely consumed in 4 h. Upon completion, the mixture was filtered, and the crude product was purified by column chromatography using a hexane–chloroform (8 : 2) mixture as the eluent. This process yielded a white solid of compound **1** with 80% yield, an R_f value of 0.6 (chloroform), and a melting point of 289–292 °C.[36]

2.3.2. Synthesis of 6-hydrazinyl-1*H*,1′*H*,3*H*,3′*H*-[2,2′-bibenzo[*de*]isoquinoline]-1,1′,3,3′-tetraone BIN-NHNH$_2$ (2). Hydrazine hydrate (27 mg, 0.84 mmol) was added to a stirred solution of compound **1** (200 mg, 0.42 mmol) and potassium carbonate (88 mg, 0.63 mmol) in DMF (20 ml), and the reaction was further stirred at 100 °C for 1 h. A reaction temperature of 100 °C was selected based on preliminary optimisation experiments. Temperatures below 100 °C (*e.g.*, 80–90 °C) resulted in incomplete conversion even after the reaction was carried out for a longer time, whereas temperatures above 100 °C provided no further improvement and posed a risk of decomposition of the intermediate/product. Therefore, 100 °C was identified as the optimal condition to ensure high yield and reproducibility. The progress of the reaction was monitored using thin-layer chromatography (TLC). After completion of the reaction, a brown-colored solid was obtained by adding water. Furthermore, the obtained solid was filtered and washed with cold water to obtain compound **2** in 86% yield and an R_f of 0.5 (5% ethyl acetate in chloroform).

2.3.3. Synthesis of (*E*)-6-(2-((2-hydroxynaphthalen-1-yl)methylene)hydrazinyl)-1*H*,1′*H*,3*H*,3′*H*-[2,2′-bibenzo[*de*]isoquinoline]-1,1′,3,3′-tetraone (BINNA). Compound **2** (200 mg, 0.47 mmol) and 2-hydroxy naphthaldehyde (**3**) (97 mg, 0.56 mmol) were dissolved in ethanol (35 ml) and refluxed in a round-bottom flask for 5 h. The progress of the reaction was monitored using TLC. On completion of the reaction, an orange colour solid was obtained. The orange colour solid was filtered and washed with hot ethanol to obtain pure **BINNA** with a yield of 75% and an R_f of 0.4 (10% ethyl acetate in chloroform) (Scheme 1). The structure of **BINNA** was confirmed by ^{1}H NMR (Fig. S2), ^{13}C NMR (Fig. S3) and mass spectrometry (Fig. S4). ^{1}H NMR (400 MHz, DMSO-d_6): δ ppm: 9.75 (s, 1H, CH, H_{15}), 8.51 (dd, J = 7.3 Hz, 2H, ArH, $H_{1,6}$), 8.37 (d, J = 7.9 Hz, 2H, ArH, $H_{3,4}$), 8.32 (t, J = 7.7 Hz, 2H, ArH, $H_{16,18}$), 7.96 (d, J = 9.0 Hz, 1H, ArH, H_7), 7.80 (t, J = 7.7 Hz, 4H, ArH, $H_{2,5,12,13}$), 7.78 –7.73 (m, 1H, ArH, H_9), 7.56–7.48 (m, 2H, ArH, $H_{14,17}$), 7.39–7.30 (m, 2H, ArH, $H_{10,11}$), 7.20 (d, J = 9.0 Hz, 1H, ArH, H_8); ^{13}C NMR (100 MHz, DMSO-d_6): δ ppm: 170.8, 170.7, 161.1, 160.9, 138.9, 136.2, 135.3, 135.1, 132.7, 131.9, 131.7, 129.5, 128.9, 128.3, 127.9, 127.8, 127.4, 124.5, 122.8, 122.5, 119.2, 108.6: HRMS (ESI) calcd for $C_{35}H_{20}N_4O_5$ $[M + H]^+$ 577.3180; found 577.3192 with a difference of 0.0012 and an error of 2.1 ppm, which lies well within the typical high-resolution instrument error range (±3–5 ppm), confirming the structural accuracy.

2.4. Preparation of stock solutions

Stock solutions of individual anions and metal ions were prepared in acetonitrile (CH_3CN) and distilled water at a concentration of 1×10^{-1} M. The ligand stock solution was prepared separately in a

 This journal is © The Royal Society of Chemistry 2026

Open Access Article. Published on 19 January 2026. Downloaded on 5/10/2026 5:39:47 PM. This article is licensed under a Creative Commons Attribution 3.0 Unported Licence.

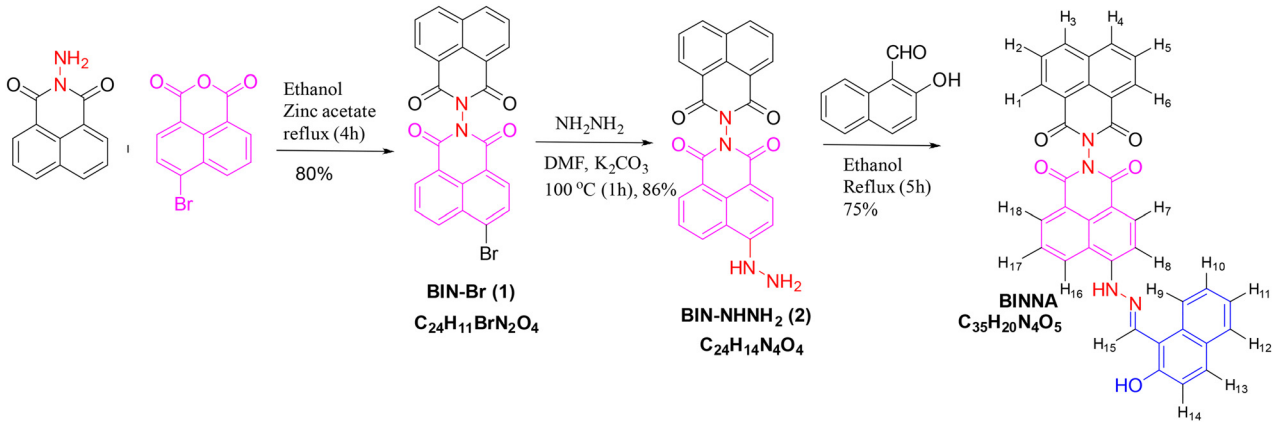

Scheme 1 Synthetic route of **BINNA**.

DMSO/CH_3CN mixture at a concentration of 1×10^{-3} M. These stock solutions were then further diluted to the required concentrations using the appropriate solvents.

2.5. Absorption and emission studies

The absorption and emission spectra of **BINNA** were analysed at a concentration of 20 μM. Absorption measurements were performed using a UV-2600 spectrophotometer and quartz cuvettes of 1 cm path length. Emission spectra were recorded with a Varian Cary Eclipse fluorescence spectrophotometer (G9800A) using slit widths of 10 nm for excitation and 20 nm for emission at the stated excitation wavelength. Time-resolved fluorescence measurements were carried out using a DeltaFlex Modular Fluorescence Lifetime Spectrofluorimeter (HORIBA Scientific – PPD-850). The stoichiometric ratios between the ligand and metal ions/nerve agent were determined using Job's plot analysis.

3. Results and discussion

3.1. Photophysical behavior of BINNA

The photophysical studies of **BINNA** were conducted using spectroscopic techniques of absorption and emission. In CH_3OH solvent, two absorption bands were displayed by **BINNA** (20 μM) at 325 and 355 nm, while weak fluorescence was observed, as shown in Fig. 2a and b. Different solvents were used to explore the spectral behaviour of **BINNA** with different polarities, such as MeOH, THF, toluene, DMF, CH_3CN, $CHCl_3$, cyclohexane, IPA, ethyl acetate, ethanol, DMSO, and hexane. No significant change in the absorption and emission spectra of **BINNA** on moving from low to high polarity was observed.

3.2. Aggregation-induced emission enhancement (AIEE) behaviour of BINNA

To investigate the aggregation behaviour of the synthesized **BINNA**, absorption and emission spectra were recorded in CH_3CN with increasing amounts of water. Initially, **BINNA** solution (20 μM in CH_3CN) displayed two absorption bands at 325 and 355 nm. As the water content was increased from 0 to 60%, a significant reduction in absorption intensity was observed. However, with further addition of water (70 to 100%), a new absorption band at 375 nm was observed along with a tail-off absorption between 500 nm and 700 nm, suggesting aggregate formation in the mixed solvent system (Fig. 3a). Fluorescence measurements further confirmed the aggregation behaviour. **BINNA** exhibited very low fluorescence intensity in pure CH_3CN, and no significant change in the fluorescence intensity was observed upon gradual addition of water up to 50% (1 : 1; H_2O : CH_3CN). Upon further incremental addition of water from 60 to 90%, a significant increase in fluorescence intensity at 380 nm was observed. In pure water, the fluorescence

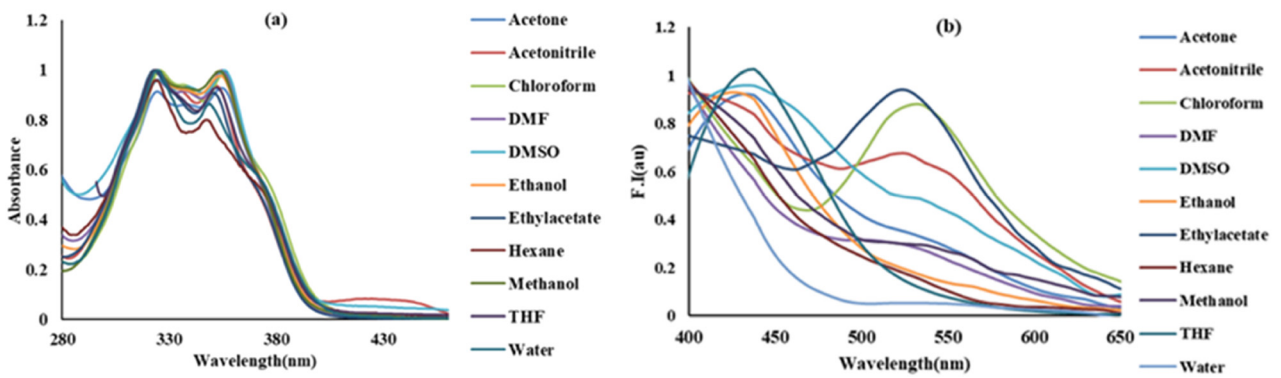

Fig. 2 (a) Absorption and (b) emission spectra of **BINNA** in different solvents.

Open Access Article. Published on 19 January 2026. Downloaded on 5/10/2026 5:39:47 PM.
This article is licensed under a Creative Commons Attribution 3.0 Unported Licence.

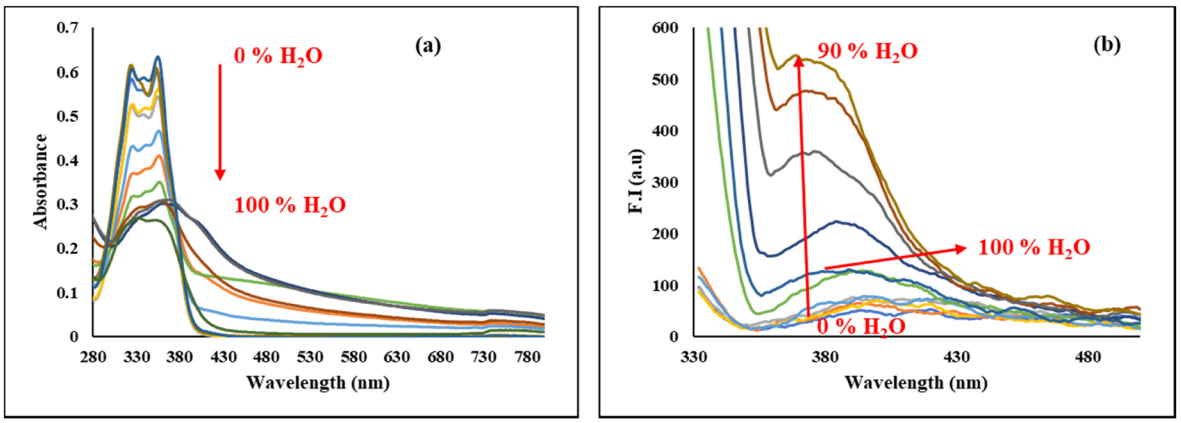

Fig. 3 (a) Absorption spectra of **BINNA** (20 μM) and (b) emission spectra of **BINNA** (20 μM) with incremental addition of H_2O in CH_3CN.

intensity of **BINNA** was quenched significantly as compared to 90% H_2O:CH_3CN (v/v), indicating significant aggregation-induced emission enhancement effects (Fig. 3b). These results confirmed the formation of aggregates upon increasing water concentration.

A dynamic light scattering (DLS) study was conducted to explore how varying water content influences the particle size and aggregation behaviour of **BINNA**. In pure acetonitrile (CH_3CN), **BINNA** displayed a relatively uniform particle size, averaging 145 ± 3 nm, with a polydispersity index (PDI) of 0.372 (Fig. 4a). However, as water was incrementally introduced into the system, a clear trend of particle growth emerged, signifying enhanced aggregation. At 50 : 50 H_2O : CH_3CN ratio, the average hydrodynamic diameter expanded to 844 ± 10 nm, accompanied by a PDI of 0.479 (Fig. 4b). Further increasing the water content to 70% resulted in an increase of particle size to 1185 ± 16 nm, with a PDI of 0.587 (Fig. 4c). Moreover, at a water content of 90%, the particle size of **BINNA** increased to 2608 ± 8 nm (Fig. 4d), and in pure water, **BINNA** exhibited an average particle size of 3092 ± 10 nm with a PDI value of 0.717 (Fig. 4e). This progressive increase in both particle size and PDI underscores the aggregation of **BINNA** in aqueous environments, suggesting a growing heterogeneity in particle size distribution as the water content increases.

Furthermore, to explore how water content influences the structure of **BINNA**, FE-SEM images were recorded with increasing concentration of water in CH_3CN. FE-SEM clearly demonstrated that the particle size increased with a higher H_2O ratio. In a pure CH_3CN environment, **BINNA** displayed small rod-like mixed morphology, *i.e.*, small needle-like as well as rod-like shapes with particle size between 130 and 140 nm (Fig. 5a). However, upon increasing the water content to 50%, these

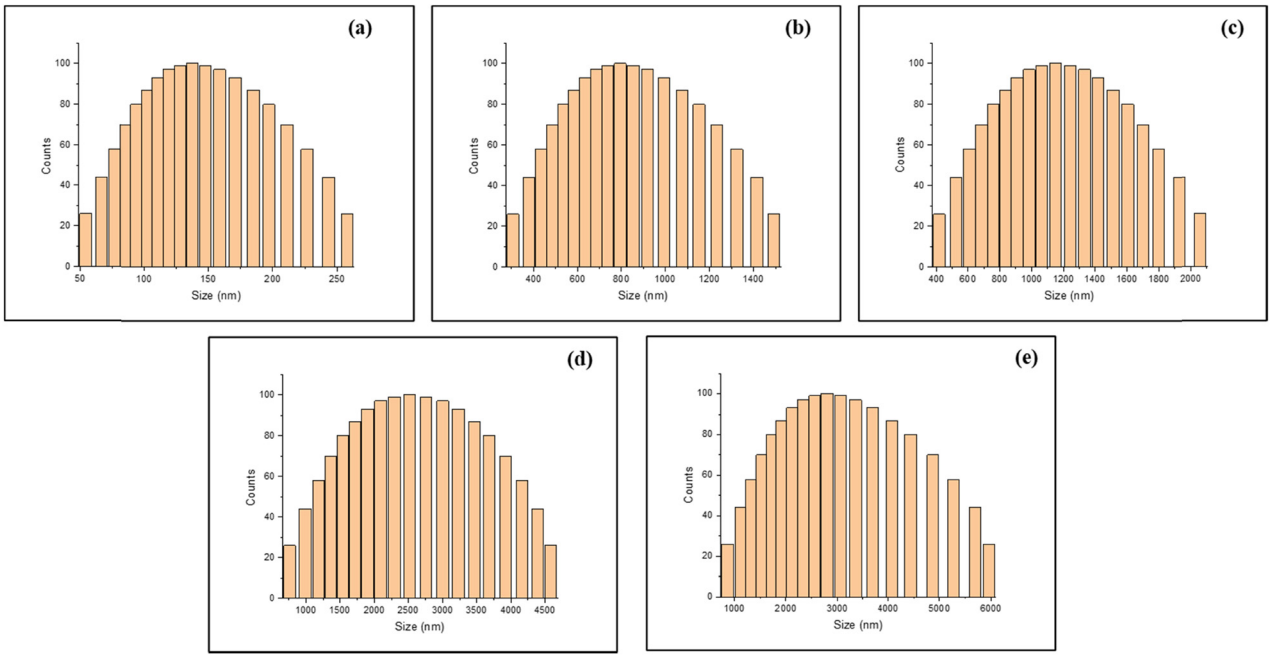

Fig. 4 Hydrodynamic size of **BINNA** in (a) CH_3CN, (b) 50% H_2O, (c) 70% H_2O, (d) 90% H_2O and (e) H_2O only.

 This journal is © The Royal Society of Chemistry 2026

Open Access Article. Published on 19 January 2026. Downloaded on 5/10/2026 5:39:47 PM. This article is licensed under a Creative Commons Attribution 3.0 Unported Licence.

small rod-like structures start accumulating together to form aggregates with a particle size between 800 and 870 nm; hence, an increase in size can be observed (Fig. 5b). Furthermore, upon increasing the water concentration to 90%, **BINNA** exhibited an elongated rod-like structure with a particle size between 2400 and 2800 nm and a diameter between 180 and 220 nm, clearly indicating an increase in the particle size of **BINNA** (Fig. 5c), whereas in pure water, these rod structures started accumulating, leading to the formation of aggregates with a particle size between 3000 and 3300 nm (Fig. 5d). The particle size determined from FE-SEM and DLS were consistent. These evolving structures indicate the progressive self-assembly and aggregation of the molecules.

To further elucidate the aggregation-induced emission enhancement (AIEE) behavior of **BINNA**, time-correlated single photon counting (TCSPC) measurements were conducted by varying the water content in CH_3CN. Initially, in pure CH_3CN, **BINNA** displayed an average fluorescence lifetime of 0.42 ns, having three decay components with lifetimes and populations of 0.81 ns and 3%, 4.15 ns and 2%, and 0.24 ns and 95% (Table 1). Upon increasing the water content to 50%, *i.e.*, $CH_3CN:H_2O$ (1 : 1), a noticeable increase in the average lifetime of **BINNA** was observed with a lifetime value of 0.57 ns, corresponding to three decay components with lifetimes and populations of 0.57 ns and 50%, 1.18 ns and 0%, and 0.57 ns and 50%. Furthermore, a significant enhancement in the average fluorescence lifetime of **BINNA** was observed upon increasing the water content to 90% ($CH_3CN:H_2O$ = 1 : 9), with lifetime reaching 1.06 ns, having three decay components with lifetimes and populations of 0.46 ns and 0%, 1.06 ns and 50%, and 1.06 ns and 50%. In pure water, the lifetime of **BINNA** was decreased and the average lifetime was found to be 0.51 ns with three decay components having lifetime and population values of 0.56 ns and 63%, 1.44 ns and 6%, and 0.29 ns and 31%. The progressive enhancement in fluorescence lifetime with increasing water content suggests the formation of molecular aggregates, leading to an enhancement of the excited state. The enhancement of fluorescence lifetime (from 0.42 ns to 1.06 ns) with increasing water content is a direct consequence of the molecular packing mode. The formation of intermolecular π–π stacked aggregates in the poor solvent (high water content) restricts the intramolecular rotation, which, in turn, reduces the non-radiative transitions and enhances the probability of

Table 1 Fluorescence lifetime measurements of **BINNA** with increasing concentration of water

	τ_1 (ns)	τ_2 (ns)	τ_3 (ns)	α_1	α_2	α_3	τ_{av} (ns)	χ^2
CH_3CN	0.81	4.15	0.24	0.03	0.02	0.95	0.42	1.10
$CH_3CN:H_2O$ (1 : 1)	0.57	1.88	0.57	0.50	0.00	0.50	0.57	1.05
$CH_3CN:H_2O$ (1 : 9)	0.46	1.06	1.06	0.00	0.50	0.50	1.06	0.99
H_2O	0.56	1.44	0.29	0.63	0.06	0.31	0.51	1.11

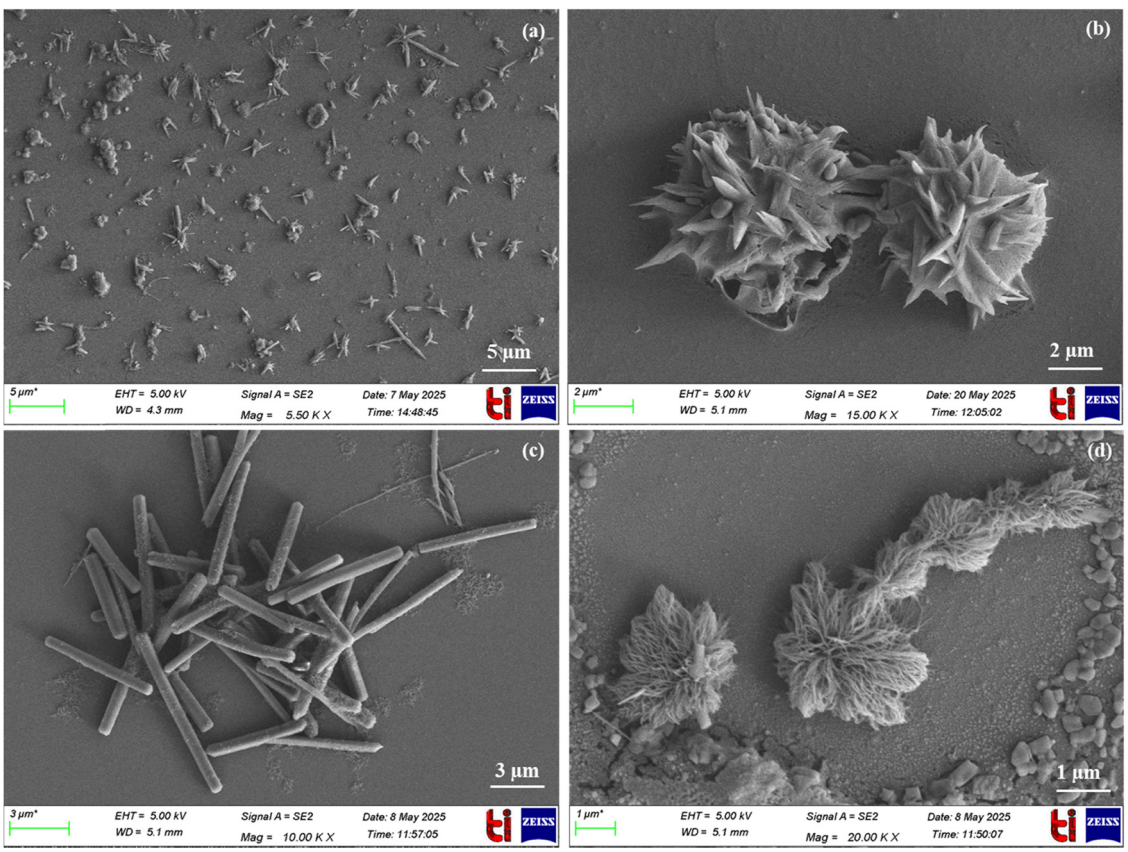

Fig. 5 FE-SEM images of **BINNA** in (a) CH_3CN; (b) 50% ($H_2O:CH_3CN$); (c) 90% ($H_2O:CH_3CN$); and (d) H_2O only.

Open Access Article. Published on 19 January 2026. Downloaded on 5/10/2026 5:39:47 PM. This article is licensed under a Creative Commons Attribution 3.0 Unported Licence.

radiative decay, thereby increasing the fluorescence lifetime. These findings are consistent with the results obtained from steady-state fluorescence, dynamic light scattering (DLS), and scanning electron microscopy (SEM), collectively reinforcing the hypothesis of aggregation-induced emission enhancement in **BINNA**.

3.3. Sensing properties of BINNA towards metal ions

3.3.1. Absorption behaviour in the presence of different metal ions. UV-visible spectroscopy was used to evaluate the metal ion-sensing capability of **BINNA**. Initial screening was carried out in various solvents, including CH_3CN, CH_3OH, H_2O, and their mixtures. Among these, MeOH yielded the most promising results, showing both high sensitivity and selectivity. Consequently, further investigations were conducted using MeOH as a solvent system.

To assess metal ion detection, UV-vis absorption spectra of **BINNA** (20 μM, MeOH) were recorded in the absence and presence of various metal ions, including Cu^{2+}, Ni^{2+}, Ga^{3+}, Al^{3+}, Pb^{2+}, Mg^{2+}, Cr^{3+}, Mn^{2+}, Fe^{3+}, Co^{2+}, Zn^{2+}, Na^{+}, and Hg^{2+} (Fig. 6a and c). In its native state, **BINNA** exhibited two absorption bands at 325 and 355 nm. Upon the addition of aluminium ions (Al^{3+}), a new band at 340 nm along with a red shift was observed, with the emergence of a new absorption band at 408 nm, accompanied by a noticeable light-yellow colour visible to the naked eye (Fig. 6d), whereas no significant spectral change was observed with other metal ions, suggesting that **BINNA** exhibits selectivity towards Al^{3+} ions. Further titrations with increasing concentrations of Al^{3+} ions (0–43 μM) revealed a gradual increase in the absorption band at 338 nm and the concurrent appearance of a 408 nm band, along with a clear isosbestic point at 388 nm, indicating the presence of two or more species in dynamic equilibrium at that wavelength (Fig. 6b).

3.3.2. Fluorescence response towards different metal ions. The fluorescence response of **BINNA** (20 μM, MeOH) to various

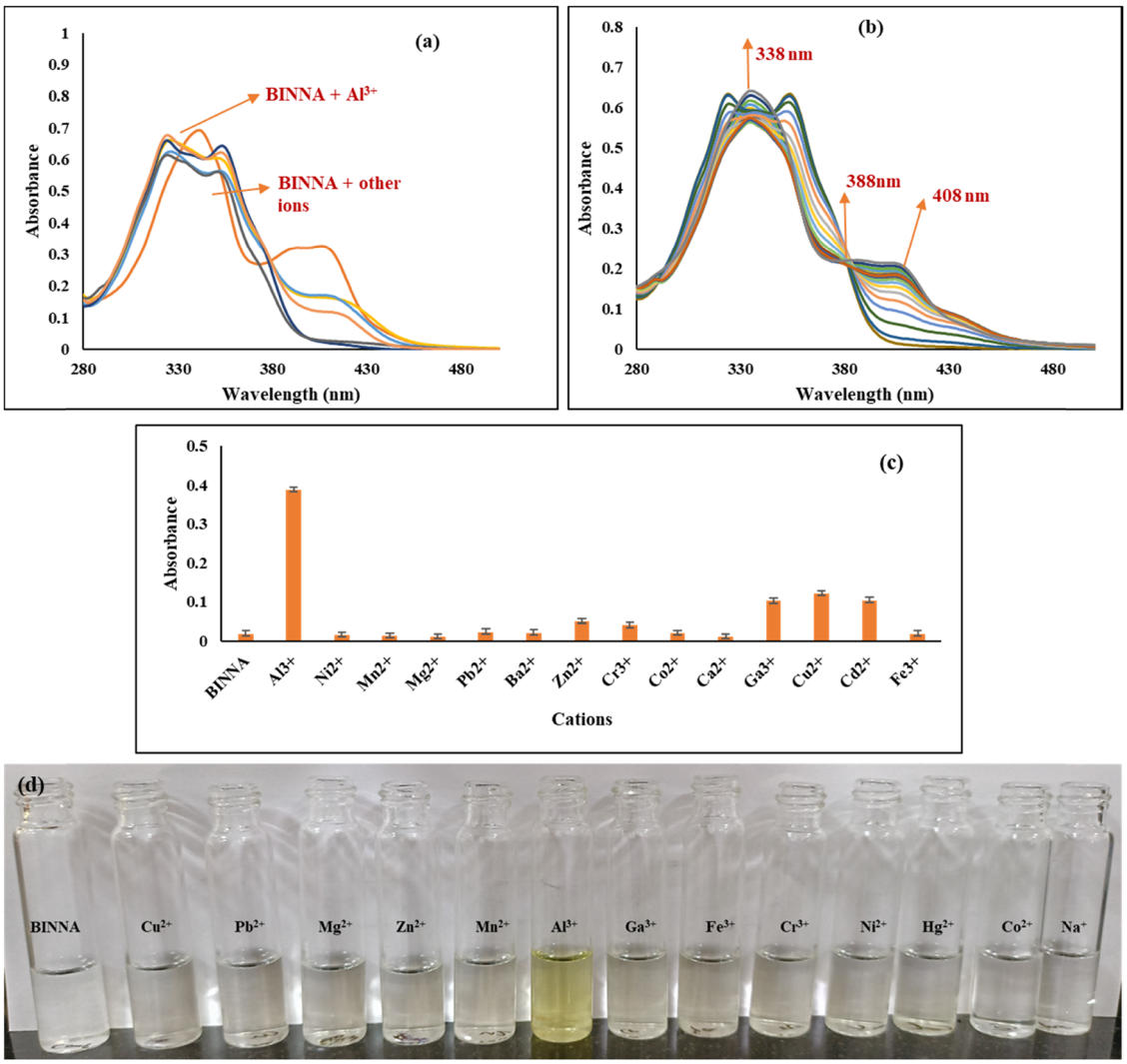

Fig. 6 (a) UV-vis absorption spectra of **BINNA** (20 μM, CH_3OH) in the presence and absence of metal ions (1000 μM). (b) Variation in the absorption spectra of **BINNA** (20 μM) on gradual addition of Al^{3+} ions at a concentration of 0–43 μM in CH_3OH. (c) Bar graph representation of the change in the absorbance of **BINNA** in the presence and absence of metal ions at 408 nm. (d) Visible color change of **BINNA** after adding different metal ions.

 This journal is © The Royal Society of Chemistry 2026

Open Access Article. Published on 19 January 2026. Downloaded on 5/10/2026 5:39:47 PM. This article is licensed under a Creative Commons Attribution 3.0 Unported Licence.

metal ions such as Cu^{2+}, Ni^{2+}, Ga^{3+}, Al^{3+}, Pb^{2+}, Mg^{2+}, Cr^{3+}, Mn^{2+}, Fe^{3+}, Co^{2+}, Zn^{2+}, Na^{+}, and Hg^{2+} (Fig. 7a and c) was investigated using steady-state fluorescence spectroscopy to evaluate its sensing capability in the excited state. In MeOH, **BINNA** exhibited a weak fluorescence emission at 405 nm when excited at 325 nm with a quantum yield (Φ_f) of 0.11. However, the addition of aluminium ions (Al^{3+}) led to a significant increase in emission intensity at 450 nm, whereas no significant change was observed in the presence of other metal ions. The probe exhibited a remarkable fluorescence enhancement specifically toward Al^{3+}, with the emission intensity at 450 nm increasing by more than 21-fold compared to other metal ions with a quantum yield (Φ_f) of 0.85. The result inferred that **BINNA** displays excellent selectivity toward Al^{3+} ions. A visible colour change, along with enhanced fluorescence under UV light, was also observed (Fig. 7d). To further understand this interaction, spectrofluorimetric titrations were conducted in the presence of Al^{3+}. As the concentration of Al^{3+} ions increased from 0 to 43 μM, the fluorescence intensity of **BINNA** progressively increased, corresponding to the emission band at 450 nm (Fig. 7b). This enhancement depicted the efficient binding of Al^{3+} ions with **BINNA**.

3.3.3. Detection limit of BINNA and interference studies towards Al^{3+} ions. The linear plot of Al^{3+} *versus* fluorescence intensity was used to calculate the detection limit. The detection limit of **BINNA** towards Al^{3+} ions was found through fluorimetric titration profiles and determined to be 18.2 nM (Fig. S5). This low detection limit makes the fluorescence probe suitable for detecting Al^{3+} in biological and environmental samples. The permissible limit of Al^{3+} in drinking water, as established by the WHO, is 7.41 μM. Therefore, the observed detection value is considerably lower, indicating the exceptional sensitivity of the probe towards Al^{3+}. To assess the selectivity of **BINNA** for Al^{3+}, interference studies were conducted by mixing **BINNA** and Al^{3+} (10 μM) in MeOH and introducing 10 μM of various competing metal ions. We also checked the selectivity of **BINNA** for Al^{3+} ions in the presence of a higher concentration of interfering ions (50 μM). These interfering ions had no significant effect on the detection of Al^{3+} at 450 nm (Fig. 7e and Fig. S6), indicating that **BINNA** exhibits strong selectivity and practical applicability for detecting Al^{3+} in the presence of other cations.

3.4. Sensing properties of BINNA towards anions and nerve agents

3.4.1. Absorption response towards anions and nerve agents. As the probe **BINNA** displayed promising results in MeOH towards metal ions, we investigated the sensing ability of **BINNA** towards various anions and nerve agent mimics in MeOH. To evaluate the detection capability for anions and nerve agents, UV-vis absorption spectra of **BINNA** were measured in both the absence and presence of anions and nerve agents, including CN^-, SCN^-, Br^-, CH_3COO^-, $H_2PO_4^-$, HSO_4^-, F^-, Cl^-, I^-, $P_2O_7^{4-}$, S^{2-}, DCP, TEP and TBP (Fig. 8a). In its unbound state, **BINNA** displayed two absorption peaks at 325 and 355 nm. The absorption band at 325 nm disappeared with the formation of a new band at 335 nm, and the absorption band intensity corresponding to 355 nm was decreased in the presence of DCP. On the other hand, anions and other nerve agents did not display notable spectral changes, indicating that **BINNA** demonstrates exceptional selectivity for DCP only. Progressive titrations with increasing concentrations of DCP, ranging from 0 to 38 μM, showed a steady depletion of the absorption band at 325 nm, along with the appearance of a new absorption band at 335 nm, while the absorption band at 355 nm was gradually decreased (Fig. 8b).

3.4.2. Fluorescence response towards different anions and nerve agents. To explore the excited-state sensing potential of **BINNA**, its fluorescence response toward various anions and nerve agents, including CN^-, SCN^-, Br^-, CH_3COO^-, $H_2SO_4^-$, HSO_4^-, F^-, Cl^-, I^-, $P_2O_7^{4-}$, S^{2-}, DCP, TEP and TBP, was evaluated using steady-state fluorescence spectroscopy (Fig. 8c and e). Upon excitation of the free probe at 325 nm, no subsequent emission band was observed, indicating that the free probe is in its quenched state with a quantum yield (Φ_f) of 0.12. Remarkably, the introduction of DCP triggered a dramatic fluorescence enhancement, exhibiting an emission band at 371 nm. None of the other tested anions and nerve agents exhibited a comparable response. The probe displayed a remarkable fluorescence enhancement specifically toward DCP, with the emission intensity increasing 22-fold more than that of other metal ions at 371 nm and a quantum yield (Φ_f) of 0.79. The result inferred that **BINNA** displays excellent selectivity toward DCP, highlighting **BINNA**'s exceptional selectivity for DCP. To investigate deeper into the mechanism of this interaction, spectrofluorimetric titrations were performed. With incremental additions of DCP ranging from 0 to 38 μM, a consistent increase in emission intensity at 371 nm was recorded (Fig. 8d), indicating a strong and efficient complexation between **BINNA** and DCP. This progressive enhancement underscores the potential of **BINNA** as a highly responsive fluorescent probe for DCP detection.

3.4.3. Binding efficiency towards DCP. To gain deeper insights into the interaction affinity between **BINNA** and DCP, the binding constant for the **BINNA**–DCP complex was determined using the Benesi–Hildebrand method. By plotting $1/(I - I_0)$ against 1/[DCP], a linear relationship was established, yielding a binding constant of 4.5×10^4 M^{-1} for DCP (Fig. S7a). The result shows that the fluorescence intensity increased almost linearly with incremental addition of DCP up to 38 μM. Impressively, the detection limit was calculated to be as low as 8.5 nM, underscoring the remarkable sensitivity of **BINNA** as a fluorescence-based probe (Fig. S7b). Further investigation into the binding stoichiometry was carried out through fluorescence titrations. A maximum emission intensity was observed at a molar ratio of 0.5, indicating a 1 : 1 binding mode between **BINNA** and DCP (Fig. S7c).

To validate **BINNA**'s selectivity, interference studies were performed by co-incubating **BINNA** with DCP (10 μM) in methanol, followed by the addition of various competing nerve agents and anions at equivalent concentrations (10 μM). We further checked the selectivity of **BINNA** for DCP ions in the presence of a higher concentration of interfering ions (50 μM).

Open Access Article. Published on 19 January 2026. Downloaded on 5/10/2026 5:39:47 PM.
This article is licensed under a Creative Commons Attribution 3.0 Unported Licence.

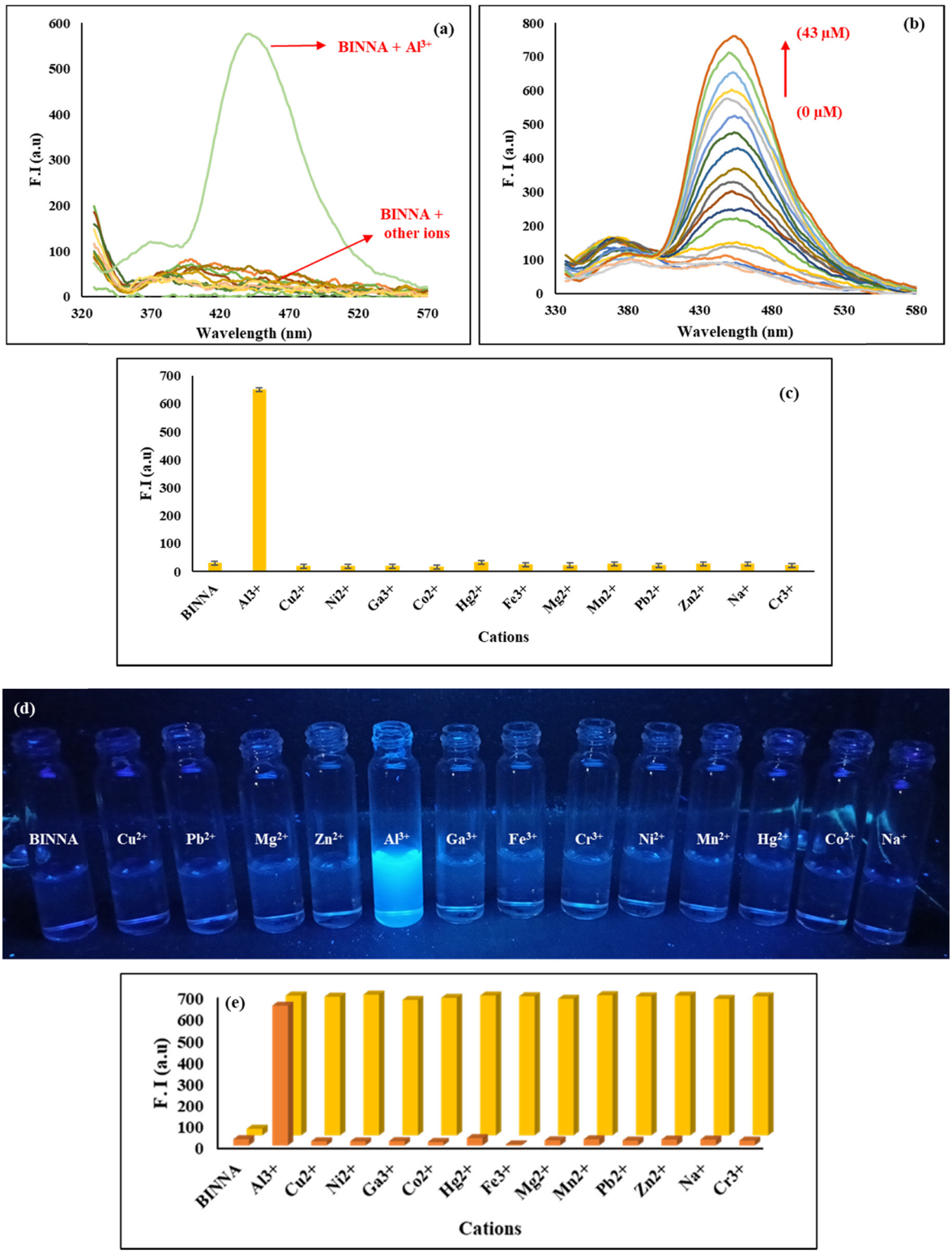

Fig. 7 (a) Fluorescence spectra of **BINNA** (20 μM, CH_3OH) with and without 1000 μM of cations added. (b) Variation in the fluorescence intensity of **BINNA** (20 μM) on gradual addition of Al^{3+} ions at a concentration of 0–43 μM in CH_3OH. (c) Bar graph representation of the fluorescence change of **BINNA** in the presence and absence of metal ions at 450 nm. (d) Fluorescence color change of **BINNA** after adding different metal ions under UV light. (e) The relative intensity of **BINNA** at 450 nm in the presence and absence of Al^{3+} ions (10 μM), while considering various competing metal ions (10 μM). The change in the emission intensity of **BINNA** with different metal ions is represented by orange bars, whereas yellow bars represent the changes in the emission intensity of **BINNA** in the presence of Al^{3+} ions and different competing ions.

 This journal is © The Royal Society of Chemistry 2026

Open Access Article. Published on 19 January 2026. Downloaded on 5/10/2026 5:39:47 PM.
This article is licensed under a Creative Commons Attribution 3.0 Unported Licence.

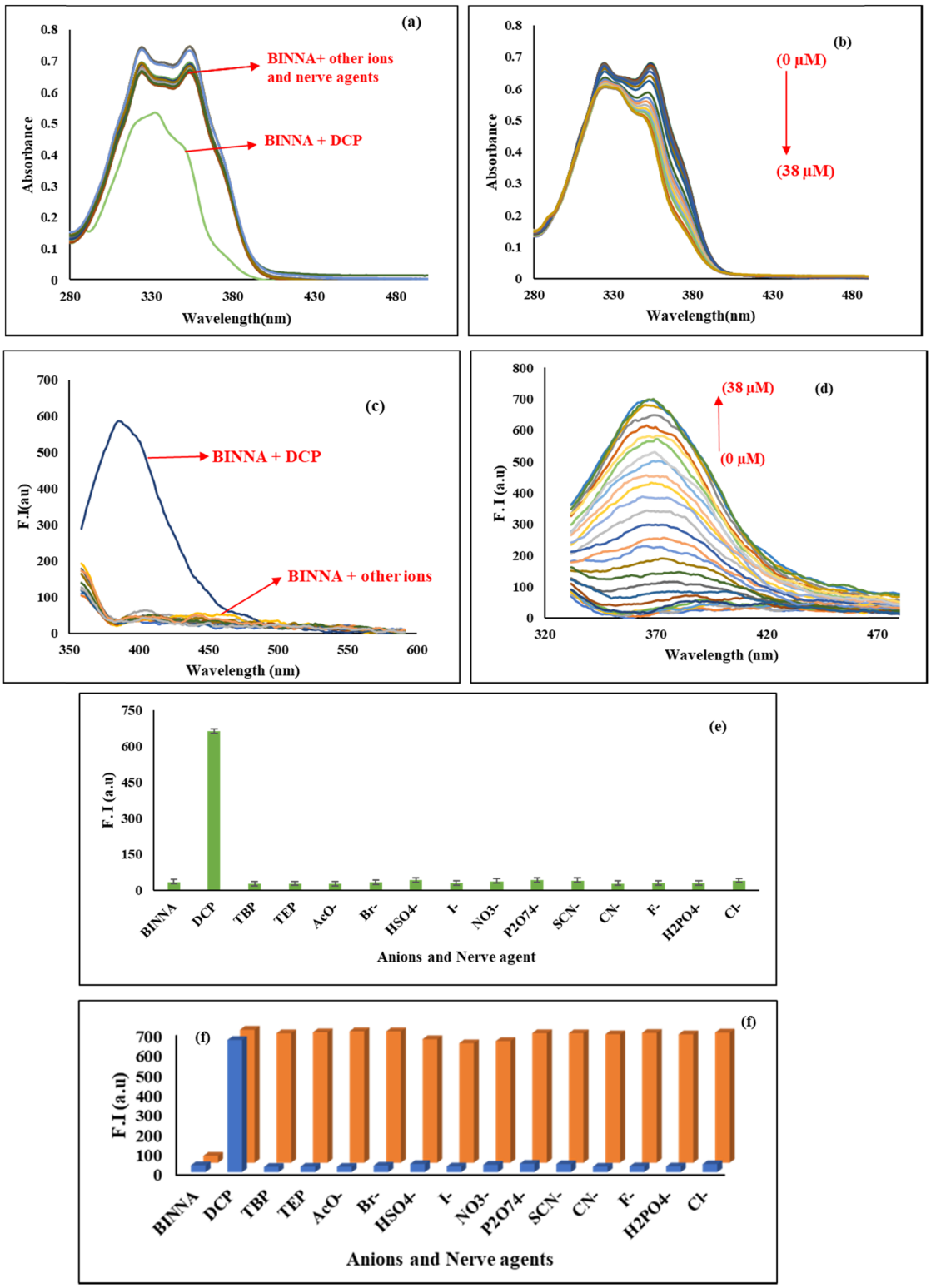

Fig. 8 (a) UV-vis absorption spectra of **BINNA** (20 µM, CH_3OH) in the presence and absence of 1000 µM of anions and nerve agents. (b) Variation in the absorption spectra of **BINNA** (20 µM) on progressive addition of DCP (0–38 µM) in CH_3OH. (c) Fluorescence spectra of **BINNA** in the absence and presence of anions and nerve agents (1000 µM). (d) Fluorescence intensity variation of **BINNA** (20 µM) on gradual addition of DCP at a concentration of 0–38 µM in CH_3OH. (e) Bar graph representation of the fluorescence changes of **BINNA** in the presence and absence of anions and nerve agents at 371 nm. (f) Relative intensity of **BINNA** at 371 nm in the presence and absence of DCP (10 µM) with several anions (10 µM). The fluorescence intensity change of **BINNA** with different anions and nerve agents is represented by blue bars, and orange bars represent **BINNA**–DCP in the presence of different competing ions and nerve agents.

Open Access Article. Published on 19 January 2026. Downloaded on 5/10/2026 5:39:47 PM. This article is licensed under a Creative Commons Attribution 3.0 Unported Licence.

The fluorescence signal at 371 nm remained virtually unaffected (Fig. 8f and Fig. S8), clearly demonstrating that **BINNA** maintains high reliability in DCP detection even in the presence of potentially disruptive nerve agents and anions. This robust selectivity, combined with its low detection limit, reinforces **BINNA**'s utility as a reliable and high-performance sensor for DCP.

3.5. Time-dependent study of BINNA

The response time of a fluorescence probe is crucial for the real-time detection of cations and nerve agents. Accordingly, time-dependent emission studies were performed to evaluate the response of **BINNA** toward Al^{3+} ions and DCP. As shown in Fig. 9, **BINNA** displayed weak fluorescence at 405 nm in the absence of Al^{3+} ions and DCP, with no significant change over time. However, upon the introduction of DCP, a pronounced increase in fluorescence intensity at 370 nm was observed, reaching a steady plateau within 40 s, whereas, upon the introduction of Al^{3+} ions, a marked increase in emission intensity at 450 nm was observed, reaching a steady plateau within 100 s. This rapid enhancement clearly demonstrates the fast response of the **BINNA** probe toward DCP and Al^{3+} ions, confirming its suitability for real-time detection applications.

3.6. Plausible mechanism

Furthermore, to gain insight into the mode of interaction of **BINNA** with Al^{3+} ions and DCP, we recorded the HRMS spectra of **BINNA** in the absence and presence of Al^{3+} ions and DCP. The mass spectrum of free **BINNA** displayed an *m*/*z* peak of 577.3213 $(M + H)^+$, whereas upon the addition of Al^{3+} ions to the solution of **BINNA**, the peak corresponding to the mass of **BINNA** at *m*/*z* 577.3213 diminished with the appearance of new peaks at *m*/*z* 194.9906 corresponding to the mass of compound **3** + Na^+, whereas the peak at *m*/*z* 273.0049 corresponds to the mass of compound **3** + Al^{3+} + CH_3OH + CH_3CN and the peak at *m*/*z* 459.9230 is the peak corresponding to the mass of compound **2** + $2H_2O$. These results inferred that **BINNA** is hydrolyzed in the presence of Al^{3+} ions (Fig. S9). We also recorded the absorption and emission spectra of **BINNA**, **BINNA** + Al^{3+} and compound **3** to support the hydrolysis of **BINNA** in the presence of Al^{3+} ions (Fig. S10). The results of absorption and emission spectroscopy are in accordance with the HRMS results of **BINNA** in the presence of Al^{3+} ions.

Furthermore, in the presence of DCP, new peaks at *m*/*z* 733.1271 corresponding to the mass of **4** + H_2O and one peak at *m*/*z* 753.0900 corresponding to the mass of **4** + CH_3CN were observed. These results indicated that DCP binds with **BINNA** in a 1 : 1 stoichiometry (Fig. S11). The plausible mechanisms for the detection of Al^{3+} ions and DCP by **BINNA** are shown in Fig. 10.

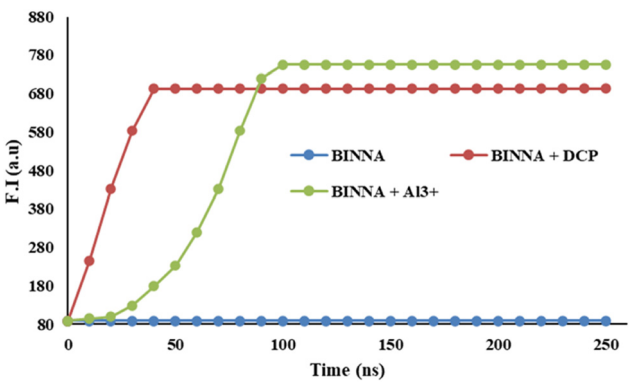

Fig. 9 Time-dependent fluorescence response of **BINNA** upon the addition of Al^{3+} and DCP.

3.7. Time-correlated single photon counting (TCSPC) study

To gain further understanding of **BINNA**'s interaction with Al^{3+} ions and DCP at 325 nm, a time-correlated single photon counting (TCSPC) experiment was conducted. Both **BINNA** and its complexes with Al^{3+} ions and DCP exhibited tri-exponential decay profiles, suggesting the presence of three distinct decay pathways (Fig. S12). For **BINNA** alone, three decay components with lifetime values of 1.38 ns, 6.20 ns, and 0.25 ns and populations of 18%, 7%, and 75% were observed, resulting in an average lifetime of 0.85 ns (Table 2). Upon interaction with DCP, the same three decay components were obtained with lifetimes of 0.81 ns, 5.10 ns, and 0.13 ns and populations of 3%, 4%, and 94%, with an average lifetime of 0.32 ns. Similarly, upon the addition of Al^{3+} ions, the complex also exhibited three decay components with lifetime values of 1.27 ns, 0.32 ns, and 5.90 ns and populations of 29%, 68%, and 3%, respectively, having an average lifetime value of 0.79 ns. The average lifetime of **BINNA** changed largely upon interaction with Al^{3+} and DCP, suggesting that its binding with metal ions and nerve agents occurred through a purely dynamic mechanism.

3.8. Theoretical studies

The ground-state optimized geometries of **BINNA** and its derivative **BINNA**·DCP are shown in Fig. 11. Additionally, three low-lying Franck–Condon excitations (FCEs) were computed at S_0 geometry, as summarized in Table 3. The time-dependent density functional theory (TDDFT) calculations revealed $S_0 \rightarrow S_1$ excitation at 397 nm (experimental $\lambda_{max} \approx 355$ nm), primarily comprising HOMO → LUMO+1 (~60%) and HOMO → LUMO (~24%) transitions, with an oscillator strength of 1.1718. Molecular orbital analysis indicates electron density transfer from the naphthaldehyde moiety (HOMO) to the naphthalimide moiety (LUMO+1), suggesting an intramolecular charge transfer (ICT) process. This is supported by hole–electron analysis showing a modest spatial overlap (Sr = 0.69183) and a centroid separation of 1.676 Å. Additional transitions, $S_0 \rightarrow S_2$ and $S_0 \rightarrow S_3$, were calculated at 316 nm and 303 nm, with oscillator strengths of 0.0967 and 0.3561, respectively. Solvent effects (chloroform, acetone, DMSO, and methanol) produced only minor spectral shifts (392–399 nm) and the corresponding dipole moment variations (4.52–5.38 D), though these modest shifts appreciably influence emission behaviour (Table S2).

The molecular electrostatic potential (MEP) analysis identifies significant negative regions at the oxygen atoms of the naphthalimide and naphtholic units, indicating sites of electrophilic attack, while positive potential regions are localized around

 This journal is © The Royal Society of Chemistry 2026

Open Access Article. Published on 19 January 2026. Downloaded on 5/10/2026 5:39:47 PM.
This article is licensed under a Creative Commons Attribution 3.0 Unported Licence.

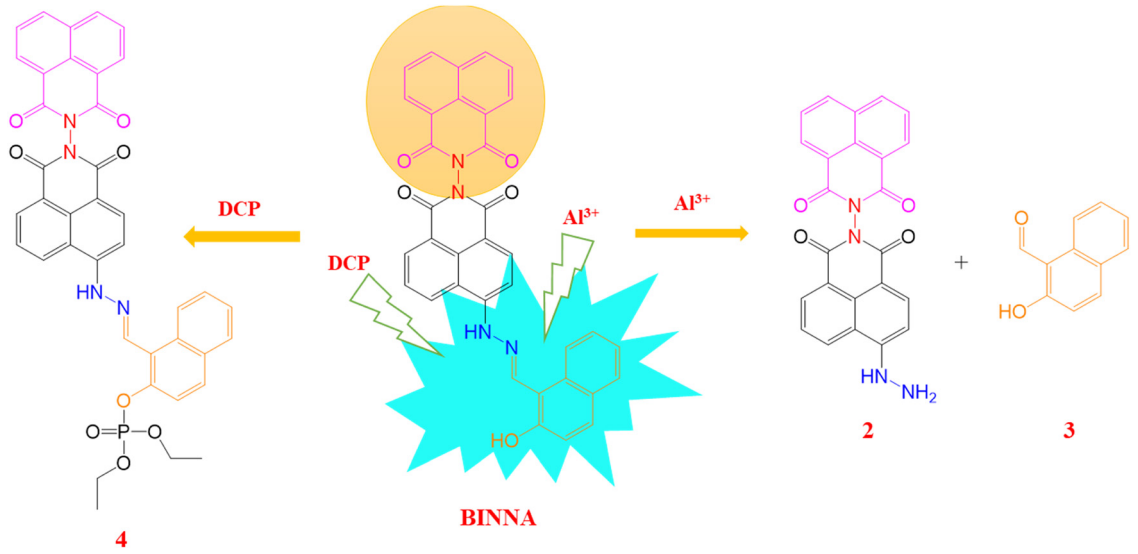

Fig. 10 Plausible mechanisms for the detection of Al^{3+} ions and DCP.

Table 2 Fluorescence lifetime measurements of **BINNA** and its complexes with DCP and Al^{3+}

	τ1 (ns)	τ2 (ns)	τ3 (ns)	α1	α2	α3	χ^2	τav (ns)
BINNA	1.38	6.20	0.25	0.18	0.07	0.75	1.09	0.85
BINNA + DCP	0.81	5.10	0.13	0.03	0.04	0.94	1.03	0.32
BINNA + Al^{3+}	1.27	0.32	5.90	0.29	0.68	0.03	1.12	0.79

hydrogen atoms attached to the naphthalene, azine, and terminal naphthalimide rings, possible sites for nucleophilic interactions (Fig. 11). The analysis further suggests that the DCP analyte can engage in electrophilic interaction with the hydroxyl group on the naphthol ring.

Following geometry optimization of **BINNA**·DCP, TDDFT computations of electronic spectra show $S_0 \rightarrow S_1$ excitation at 390 nm, with dominant contributions from HOMO → LUMO+1 (~73%) and HOMO → LUMO (~17%), and an oscillator strength of 1.1294. Similar to **BINNA**, this excitation reflects electron density migration from the naphthaldehyde to the naphthalimide moiety. However, hole–electron analysis reveals slightly reduced orbital overlap (Sr = 0.67792) and increased centroid separation (D = 1.903 Å), suggesting mildly hindered ICT character upon DCP binding. $S_0 \rightarrow S_2$ and $S_0 \rightarrow S_3$ transitions in **BINNA**·DCP were computed at 305 nm and 303 nm, with oscillator strengths of 0.1507 and 0.3795, respectively. Collectively, these results elucidate the electronic structures and solvent-responsive photophysical properties of **BINNA** and **BINNA**·DCP, underscoring their ICT potential and the modulation of their excited-state characteristics by solvent effects and analyte binding.

3.9. Practical applications for the detection of Al^{3+} ions and the nerve agent

3.9.1. Cell imaging. Based on selective "turn-on" fluorescence response, the probe **BINNA** appears to be a promising

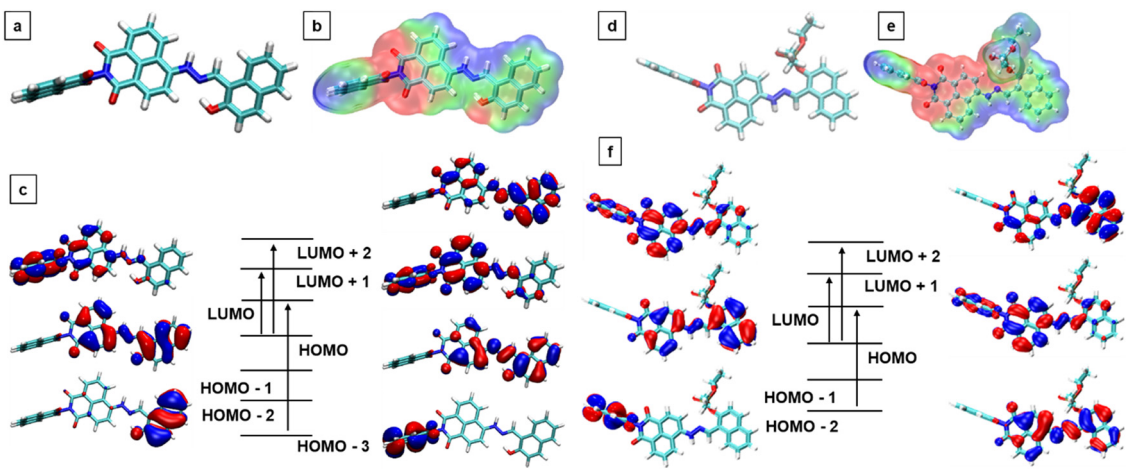

Fig. 11 Optimized structure of (a) the probe **BINNA** and (d) **BINNA**·DCP along with their molecular electrostatic potential (b) and (e) and the contributing molecular orbitals for electronic spectra: (c) the probe **BINNA** and (f) the probe **BINNA**·DCP.

Open Access Article. Published on 19 January 2026. Downloaded on 5/10/2026 5:39:47 PM.
This article is licensed under a Creative Commons Attribution 3.0 Unported Licence.

Table 3 Electronic spectral details of the probe **BINNA** and **BINNA**·DCP

Probe	Transition	Absorption peak (λ; nm)	Oscillation strength (f)	Contributing molecular orbitals (MOs, %)
BINNA-C1	$S_0 \rightarrow S_1$	397.56	1.1718	H → L + 1 (59.7%), H → L (24.3%)
	$S_0 \rightarrow S_2$	316.64	0.0967	H → L + 2 (63.6%), H-1 → L + 1 (17.5%), H-1 → L (7.6%)
	$S_0 \rightarrow S_3$	303.65	0.3561	H-3 → L (72.9%), H-3 → L + 1 (23.4%)
BINNA-C1-DCP	$S_0 \rightarrow S_1$	390.07	1.12560	H → L + 1 (73.5%), H → L (16.6%)
	$S_0 \rightarrow S_2$	305.59	0.15290	H → L + 2 (67.2%), H-1 → L + 1 (13.9%)
	$S_0 \rightarrow S_3$	303.38	0.37480	H-2 → L (81.7%), H-2 → L + 1 (13.7%)
	$S_0 \rightarrow S_1$	397.21	1.1688	H → L + 1 59.6%, H → L 24.5%

candidate for detecting Al^{3+} ions and DCP in living cells. Before cell imaging, the cytotoxicity of **BINNA** towards *E. coli* was evaluated using the MTT assay. As depicted in Fig. S13, incubation of *E. coli* with **BINNA** at various concentrations (10–50 μM)

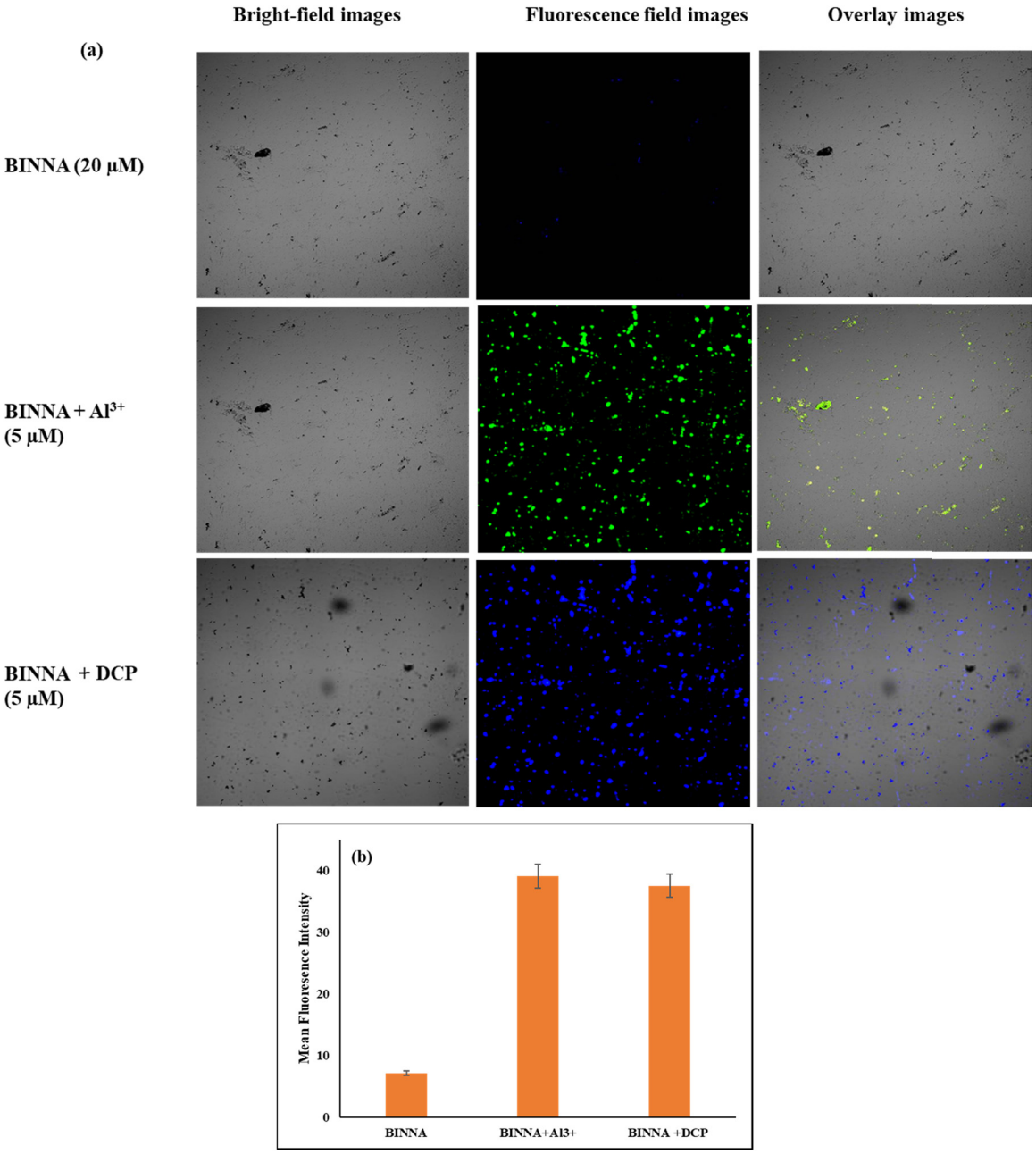

Fig. 12 (a) Bio-imaging visualisation of Al^{3+} and DCP in live *E. coli* cells using **BINNA** and (b) the corresponding fluorescence intensity graphs for (a).

 This journal is © The Royal Society of Chemistry 2026

Open Access Article. Published on 19 January 2026. Downloaded on 5/10/2026 5:39:47 PM.
This article is licensed under a Creative Commons Attribution 3.0 Unported Licence.

for 24 h resulted in over 85% survival of *E. coli* cells, indicating the biosafety of **BINNA**. To evaluate the ability of **BINNA** to image Al^{3+} and DCP in live cells, confocal fluorescence microscopy was performed using live *E. coli* cells (Fig. 12a). The cells were first incubated with **BINNA** (20 μM) for 30 minutes at 37 °C, followed by washing with PBS. Initial fluorescence imaging revealed that the cells did not exhibit discernible fluorescence after being pre-incubated with **BINNA** due to the weak fluorescence of the probe. However, when Al^{3+} (5 μM) and DCP (5 μM) were introduced to **BINNA**-treated cells and incubated for additional 10 minutes at 37 °C, a marked increase in fluorescence was observed in fluorescence images in both cases. This enhancement is likely due to the formation of complexes **BINNA**–Al^{3+} and **BINNA**–DCP. The statistical analysis of fluorescence intensity (Fig. 12b) also confirmed the high sensitivity of **BINNA** towards Al^{3+} ions and DCP. These findings indicate that **BINNA** is both cell-permeable and effective as a fluorescent sensor for detecting Al^{3+} and DCP in live cells.

3.9.2. Construction of logic devices. Recent advancements have highlighted the growing interest in supramolecular systems functioning as molecular logic gates. Among these, systems that use chemically encoded inputs and generate UV-vis or fluorescence signals as outputs have gained significant attention. In view of this, we have constructed a molecular system based on the probe **BINNA**, as it exhibits a distinct fluorescence spectral response upon interaction with DCP and Al^{3+} ions. Specifically, **BINNA** demonstrates no emission band at 370 nm and 450 nm in the absence of DCP and Al^{3+} ions, respectively. However, upon the addition of DCP, a strong emission band at 370 nm is observed, while the addition of Al^{3+} ions gives an intense emission band at 450 nm. These selective spectral responses suggest that **BINNA** is a suitable candidate for implementing molecular logic operations. DCP and Al^{3+} are designated as input signals In DCP and In Al, respectively. The corresponding outputs are monitored at λ_{em} = 450 nm (output-1) and λ_{em} = 370 nm (output-2), with threshold values set at 120 for fluorescence intensity. Signal outputs exceeding these thresholds are defined as "1" (ON), and those below as "0" (OFF), consistent with binary logic operations (Fig. 13a).

We constructed a logic circuit with two inputs (In DCP and In Al) and two outputs, measured as λ_{em} (output-1) and λ_{em} (output-2). As shown in the truth table in Fig. 13b, monitoring the emission band at 450 nm (output-1) results in an INHIBIT logic gate, where a fluorescence signal is observed only in the presence of Al^{3+} and is suppressed when DCP is concurrently present. Mechanistically, DCP possesses a highly reactive phosphonyl chloride group that can competitively react with the hydroxyl site of **BINNA** with a response time of only 40 s, forming a stable phosphorylated **BINNA**–DCP product, preventing the hydrolysis of **BINNA** in the presence of Al^{3+} as the response time for Al^{3+} to react with **BINNA** is 100 s, which is higher than that of DCP. Consequently, when both Al^{3+} and DCP are present, the fluorescence is strongly quenched ("OFF" state) at 450 nm, matching the behaviour of an INHIBIT logic gate, where DCP acts as the inhibitory input. This INHIBIT behaviour arises from a logical integration of AND and NOT operations, where the negation is applied to the input rather than the output. However, the analysis of output-2 indicates a YES logic gate response, where the presence of DCP and Al^{3+} or their combination leads to an emission band above the threshold. The integration of YES and INHIBIT gates within this molecular system enables the formation of a combinational logic circuit (Fig. 13c), demonstrating the potential of **BINNA** as a functional molecular logic element.

3.9.3. Soil sample analyses. The pronounced response of the probe **BINNA** to Al^{3+} and DCP strongly motivates us to

(a)

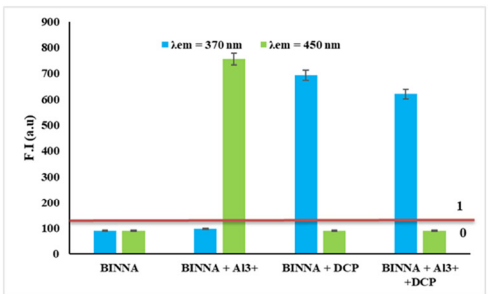

(b)

S. No	In (Al^{3+})	In (DCP)	Out-1 (λ_{em} = 450 nm)	Out-2 (λ_{em} = 370 nm)
1	0	0	0	0
2	1	0	1	0
3	0	1	0	1
4	1	1	0	1

(c)

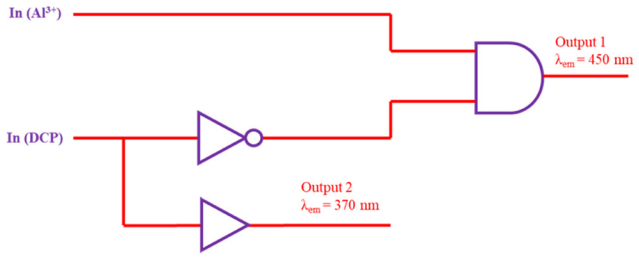

Fig. 13 (a) Emission profile at 370 and 450 nm in the presence of different inputs. (b) Truth table and (c) fabrication of a logic gate integrating YES and INHIBIT gates.

Open Access Article. Published on 19 January 2026. Downloaded on 5/10/2026 5:39:47 PM. This article is licensed under a Creative Commons Attribution 3.0 Unported Licence.

explore its practical applicability in detecting Al^{3+} and DCP within environmental soil matrices. To evaluate this potential, we investigated **BINNA**'s performance in identifying Al^{3+} and DCP in various soil types, such as sand, clay, and field soil. For this study, we followed a systematic protocol: (1) 0.5 g of each soil sample was placed in separate vials; (2) the samples were then treated with 100 μM of Al^{3+} and DCP solution and dried in air; (3) pretreated soils (0.5 g) with various concentrations of Al^{3+} and DCP were introduced into a 20 μM **BINNA** solution (2 mL in MeOH); and (4) fluorescence changes were monitored under ambient conditions.

3.9.3.1. Detection of DCP in soil samples. We evaluated **BINNA**'s ability to detect DCP in actual soil samples. Upon UV irradiation at 325 nm, all soil samples exhibited a marked fluorescence enhancement at 370 nm (Fig. 14a and Fig. S14a–c). Notably, sand samples exhibited a rapid and pronounced increase in fluorescence, while field and clay soils demonstrated progressive responses, reaching peak intensity within 10 and 20 minutes, respectively. These variations in response kinetics are attributed to intrinsic differences in soil characteristics, such as particle size, surface area, dispersibility, and light scattering behaviour in MeOH medium. Following the above procedure, the soil samples were spiked with DCP at various known concentrations, and the recovery rate was examined (Fig. S15a and Table 4). These results highlight **BINNA**'s strong potential for sensitive and selective detection of DCP in real-world environmental samples, particularly in soil contexts with recovery rates >95%.

3.9.3.2. Detection of Al^{3+} in soil samples. Furthermore, we investigated the capacity of the receptor **BINNA** to detect Al^{3+} ions in actual soil samples. Upon exposure to UV light at 325 nm, all tested soil samples displayed a significant increase in fluorescence at 450 nm (Fig. 14b and Fig. S16a–c). Among them, clay soil samples responded the fastest and most intensely, whereas field and sandy soils showed a slower, gradual rise in fluorescence. Following the above procedure, the soil samples were spiked with various known concentrations of Al^{3+} ions and the recovery rate was examined (Fig. S15b and Table 4). Overall, these findings underscore the strong capability of **BINNA** for the sensitive and selective detection of Al^{3+} in real environmental soil samples with a recovery rate > 90%.

Table 4 **BINNA** for the determination of Al^{3+} ions and DCP in real soil samples

	Al^{3+}/DCP (spiked, μM)	Al^{3+} (found, μM)	Recovery (%)	DCP (found, μM)	Recovery (%)
Sand soil	10	9.04	90.4	9.87	98.7
	20	18.24	91.2	19.54	97.7
	30	27.5	91.6	29.47	98.2
Field soil	10	9.21	92.1	9.65	96.5
	20	18.20	91.0	19.56	97.8
	30	28.55	95.1	28.98	96.6
Clay soil	10	9.43	94.3	9.75	97.5
	20	18.65	93.2	19.23	96.1
	30	28.85	96.1	29.12	97.0

4. Conclusion

In this study, we have successfully developed a bis-naphthalimide-based "turn-on" fluorescent probe, **BINNA**, for highly sensitive and selective detection of Al^{3+} ions and DCP in an MeOH solvent system, representing excellent aggregation-induced emission enhancement. **BINNA** responds distinguishably towards both analytes; upon the addition of DCP, a strong emission band at 370 nm was observed, while an intense emission band at 450 nm was observed upon the addition of Al^{3+}. **BINNA** exhibits exceptional sensing performance towards aluminium ions (Al^{3+}) and DCP with detection limits as low as 18.2 and 8.5 nm, respectively. HRMS spectra of **BINNA** were recorded in the absence and presence of the analytes to gain insight into the sensing mechanism. In addition, theoretical studies were conducted to support the experimental results. In addition to solution-based sensing, the optical properties of **BINNA** were harnessed to fabricate a logic gate by integrating "Yes" and "INHIBIT" gates using fluorescence inputs. The probe's applicability extends to real-world scenarios, successfully detecting DCP and Al^{3+} in environmental soil matrices.

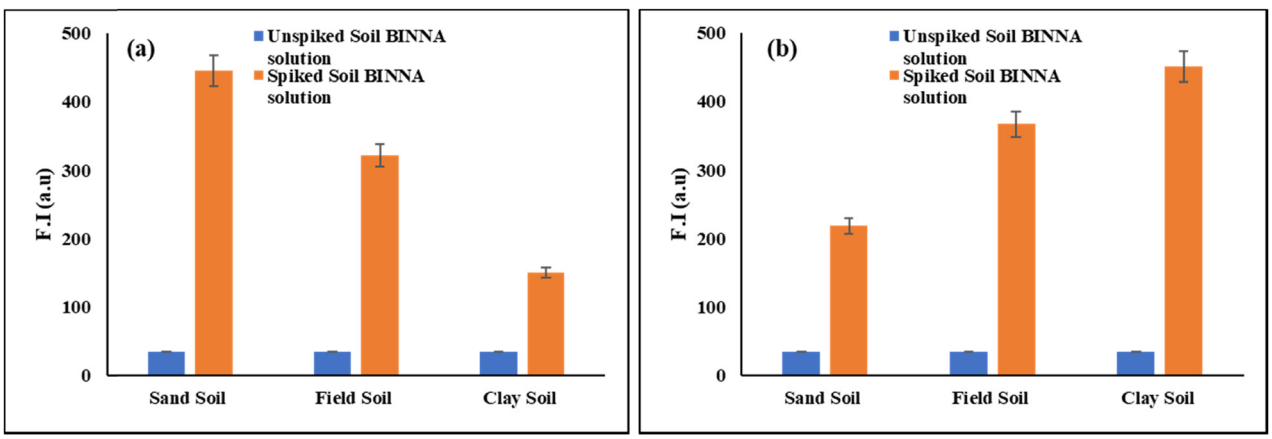

Fig. 14 The bar plots of the emission intensity unspiked and spiked (a) at 370 nm for DCP and (b) at 450 nm for Al^{3+} ions in different soil samples such as sand, field, and clay.

 This journal is © The Royal Society of Chemistry 2026

Open Access Article. Published on 19 January 2026. Downloaded on 5/10/2026 5:39:47 PM. This article is licensed under a Creative Commons Attribution 3.0 Unported Licence.

Moreover, its effectiveness in live-cell imaging of bacterial systems highlights its potential utility for environmental monitoring and bioimaging applications.

Conflicts of interest

The authors declare no competing financial interests.

Data availability

The data supporting this article have been included as part of the supplementary information (SI). Supplementary information: Material and Methods, Efficiency of **BINNA**, NMR and HRMS data. See DOI: https://doi.org/10.1039/d5tc04533a.

Acknowledgements

KP thanks the SERB, New Delhi (CRG/2023/004080), and CEEMS (Project No. TIET/CEEMS/Regular/2021/018) for providing funds. SAI Labs, Acal Lab, and TIET for NMR and DST-FIST (SR/FST/CS-II/2018/69) for HRMS analysis are also acknowledged. Authors are also thankful to Prof. Rajesh Kumar, Central University of Punjab, Bathinda, for providing confocal laser scanning microscope facility. SG thanks CEEMS/TIET for providing the fellowship.

References

1 F. Zhang, N. W. Chan, C. Liu, X. Wang, J. Shi, H. T. Kung, X. Li, T. Guo, W. Wang and N. Cao, Water Quality Index (Wqi) as a Potential Proxy for Remote Sensing Evaluation of Water Quality in Arid Areas, *Water*, 2021, **13**(22), 3250.

2 C. Immanuel David, N. Bhuvanesh, H. Jayaraj, A. Thamilselvan, D. Parimala Devi, A. Abiram, J. Prabhu and R. Nandhakumar, Experimental and Theoretical Studies on a Simple S-S-Bridged Dimeric Schiff Base: Selective Chromo-Fluorogenic Chemosensor for Nanomolar Detection of Fe^{2+} & Al^{3+} Ions and Its Varied Applications, *ACS Omega*, 2020, **5**(6), 3055–3072.

3 B. T. Ji, L. P. Liu, J. H. Chen, L. L. Gao, Y. Sun, J. J. Wang, Z. P. Deng and Y. X. Sun, Ratiometric Fluorescence Sensor Based on Dye-Encapsulated Zn-MOF for Highly Sensitive Detection of Diquat in Tap Water and Apple Samples, *Microchem. J.*, 2024, **207**, 111663.

4 T. Zangmo and A. Siripinyanond, Exploring the Applicability of Nano-Selenium for Capture of Mercury Vapor: Paper Based Sorbent and a Chemical Modifier in Graphite Furnace Atomic Absorption Spectrometry, *Anal. Chim. Acta*, 2019, **1085**, 29–38.

5 Z. P. Deng, W. Q. Hu, J. L. Yuan, Y. Sun, Q. Wang, Y. X. Sun, J. J. Wang, S. Z. Zhang and L. Xu, Dual-Ligand Zn-Based MOF as a Fluorescent Probe for the Detection of HSO^{4-}, *J. Mol. Struct.*, 2025, **1319**, 139607.

6 Z. Qin, J. A. Caruso, B. Lai, A. Matusch and J. S. Becker, Trace Metal Imaging with High Spatial Resolution: Applications in Biomedicine, *Metallomics*, 2011, **3**(1), 28–37.

7 B. Shen, xing; Qian, Y. Click Synthesis, Hg^{2+} Sensor and Intramolecular Fluorescence Resonance Energy Transfer in Novel BODIPY Dendrons, *Sens. Actuators, B*, 2017, **239**, 226–234.

8 B. Li, H. Mei, Y. Chang, K. Xu and L. Yang, A Novel Near-Infrared ''Turn-On'' Fluorescent Probe for the Detection of Fe^{3+} and Al^{3+} and Its Applications in Living Cells Imaging, *Spectrochim. Acta, Part A*, 2020, **239**, 118552.

9 A. Roy, U. Shee, A. Mukherjee, S. K. Mandal and P. Roy, Rhodamine-Based Dual Chemosensor for Al^{3+} and Zn^{2+} Ions with Distinctly Separated Excitation and Emission Wavelengths, *ACS Omega*, 2019, **4**, 6864–6875.

10 P. Srisuwan, A. Sappasombut, W. Thongyod, T. Jantarat, V. Tipmanee, N. Leesakul and D. Sooksawat, Highly Sensitive and Selective Coumarin-Based Fluorescent Chemosensor for Cu^{2+} Detection, *J. Photochem. Photobiol., A*, 2022, **427**, 113841.

11 Y. X. Sun, B. T. Ji, J. H. Chen, L. L. Gao, Y. Sun, Z. P. Deng, B. Zhao and J. G. Li, Ratiometric Emission of Tb(III)-Functionalized Cd-Based Layered MOFs for Portable Visual Detection of Trace Amounts of Diquat in Apples, Potatoes and Corn, *Food Chem.*, 2024, **449**, 139259.

12 Y. X. Sun, X. X. Li, L. L. Gan, M. X. Du, B. Zhao, W. D. Li, J. G. Li and W. K. Dong, A Novel Oligo(N,O-Donor) Fluorescent Probe Possessed the CHEF Effect for Identification of Aluminum Ions in the Environment, *Chem. Pap.*, 2024, **78**, 7001–7013.

13 X. Nan, Y. Huyan, H. Li, S. Sun and Y. Xu, Reaction-Based Fluorescent Probes for Hg^{2+}, Cu^{2+} and Fe^{3+}/Fe^{2+}, *Coord. Chem. Rev.*, 2021, **426**, 213580.

14 H. Q. Dong, T. B. Wei, X. Q. Ma, Q. Y. Yang, Y. F. Zhang, Y. J. Sun, B. B. Shi, H. Yao, Y. M. Zhang and Q. Lin, 1,8-Naphthalimide-Based Fluorescent Chemosensors: Recent Advances and Perspectives, *J. Mater. Chem. C*, 2020, **8**, 13501–13529.

15 S. Gupta, G. Kumar, V. Luxami and K. Paul, A Naphthalimide-Derived Chemosensor for Ratiometric Detection of Sulphide Ions: Insights into the S2−-Driven Reduction Cascade, Real-Time Applications and Live Cell Imaging of Bacterial Cells, *Mater. Adv.*, 2025, **6**, 4389–4401.

16 S. Rani, S. Gupta, V. Luxami and K. Paul, A Novel Target and Biomarker Benzothiazolyl-Naphthalimide Probes for Precise and Selective Detection of Serum Albumin and Anticancer Activity, *New J. Chem.*, 2022, **46**, 12082–12092.

17 S. Gupta and K. Paul, DNA Damage and Intercalation by Elinafide Modified Bis-Naphthalimides for Their Anticancer Activity, *J. Mol. Liq.*, 2023, **382**, 121980.

18 S. Gupta, V. Luxami and K. Paul, Deciphering Binding Potential of Naphthalimide-Coumarin Conjugate with c-MYC G-Quadruplex for Developing Anticancer Agents: A Spectroscopic and Molecular Modeling Approach, *ACS Appl. Bio Mater.*, 2025, **8**, 1077–1096.

19 B. Zhao, A. P. Luo, L. P. Liu, X. Bai, Y. Sun, Z. P. Deng and Y. X. Sun, A Non-Fluorescent Group-Based ''off-on-off''

Open Access Article. Published on 19 January 2026. Downloaded on 5/10/2026 5:39:47 PM. This article is licensed under a Creative Commons Attribution 3.0 Unported Licence.

Chemosensor for Detection of Al^{3+} and Fe^{3+} and Zebrafish Bioimaging, *J. Mol. Struct.*, 2025, **1327**, 141237.

20 B. Yao, J. Zhang, M. Han, L. Liang, X. Li, X. Cai and Y. Leng, Two Novel ''Turn On'' Fluorescent Probes for the Determination of Al^{3+} and Its Applications, *Inorg. Chem. Commun.*, 2023, **153**, 110798.

21 G. Kumar, I. Singh, R. Goel, K. Paul and V. Luxami, Dual-Channel Ratiometric Recognition of Al^{3+} and F^{-} Ions through an ESIPT-ESICT Signalling Mechanism, *Spectrochim. Acta, Part A*, 2021, **247**, 119112.

22 Y. Pan, P. Zhao, C. Zhou, L. Yan and X. Wu, A Dual-Functional Fluorescent Probe Based on Kaolin Nanosheets for the Detection and Separation of Aluminum Ions, *Spectrochim. Acta, Part A*, 2023, **295**, 122636.

23 J. Song, X. Yang, S. Xie, G. Zhu, X. Rao, P. Zhao and Q. Jiang, A Novel ''Turn On'' Fluorescence Probe Based on a Caffeic Acid Skeleton for Detecting Al^{3+} and Bioimaging Application, *Anal. Methods*, 2023, **15**, 3233–3239.

24 Z. Ou, M. Wang, Z. Zhang, J. Liang, J. Tang, X. Lei, L. Yang, H. Liu and L. J. Ma, A Fluorescence and Colorimetric Bifunctional Probe for Recognition of Al^{3+} and Cu^{2+} and Its Applications in Cells and Environmental Water Systems, *Microchem. J.*, 2023, **195**, 109386.

25 Q. Zhang, D. Zhang, Z. Shi, C. Jin and Y. Jiang, Construction of Naphthalimide-Based Fluorescent Probe for Sequential Detection of Al^{3+} and NOR and Its Application in Tea and Honey, *Spectrochim. Acta, Part A*, 2025, **330**, 125685.

26 N. Jain and N. Kaur, Smartphone Coupled, Solution, Solid and Vapour Phase Sensing of Nerve Agent Mimic by 1,8-Naphthalimide Derived Schiff Base, *Results Opt.*, 2023, **12**, 100466.

27 Y. He, H. Wang, C. He, R. Zeng, F. Cheng, Y. Hao, S. Chen and P. Zhang, A Porphyrin-Based Colorimetric and near Infrared Fluorescent Probe for Reversible and Rapid Detection of Diethyl Chlorophosphate, *Sens. Actuators, B*, 2025, **425**, 136983.

28 S. Rai, S. Lama, S. Pradhan, U. Darnal, J. Chourasia, S. Ahamed, N. Tohora and S. K. Das, A Donor-π-Donor Type Ratiometric Chromogenic Molecular Optode for Efficient Recognition of Sarin Analog, Diethylchlorophosphate, *J. Fluoresc.*, 2025, **35**, 11209–11219.

29 L. Zhang, K. Zhang, M. Wu, J. Ding, M. Feng, X. Li, S. Yang and H. Ma, Ultrasensitive Recognition of Trace Nerve Agents Enabled via a Thermally Activated Delayed Fluorescence-Based Fluorescent Probe, *Anal. Chem.*, 2025, **97**, 3344–3351.

30 M. Kumar, N. Kaur and N. Singh, $NiCr_2O_4$ Nanozyme-Based Portable Sensor Kit for On-Site Quantification of Nerve Agent Mimic for Environment Monitoring, *Sens. Actuators, B*, 2023, **392**, 134080.

31 F. Xiao, D. Lei, C. Liu, Y. Li, W. Ren, J. Li, D. Li, B. Zu and X. Dou, Coherent Modulation of the Aggregation Behavior and Intramolecular Charge Transfer in Small Molecule Probes for Sensitive and Long-Term Nerve Agent Monitoring, *Angew. Chem., Int. Ed.*, 2024, **63**, 00453.

32 Q. Chen, J. Liu, S. Liu, J. Zhang, L. He, R. Liu, H. Jiang, X. Han and K. Zhang, Visual and Rapid Detection of Nerve Agent Mimics in Gas and Solution Phase by a Simple Fluorescent Probe, *Anal. Chem.*, 2023, **95**, 4390–4394.

33 A. Palta, P. Thakur, G. Kumar, P. Vashisht and V. Luxami, 1,10-Phenanthroline Appended Novel Schiff Base as a Selective Fluorescent Chemosensor for Nerve Agent Stimulants, *Spectrochim. Acta, Part A*, 2025, **329**, 125601.

34 A. Palta, G. Kumar and V. Luxami, Excited State Double Proton Transfer Efficient Probe: Theoretical Investigation and Sensing Ability towards Pb^{2+} and Al^{3+} Ions, *J. Photochem. Photobiol., A*, 2022, **433**, 114198.

35 A. Palta, G. Kumar and V. Luxami, Intramolecular Dual Hydrogen Bonded Fluorescent ''Turn-On'' Probe for Al^{3+} and HSO^{4-} Ions: Applications in Real Water Samples and Molecular Keypad Lock, *Spectrochim. Acta, Part A*, 2023, **300**, 122873.

36 S. Gupta, V. Luxami and K. Paul, Bacterial Cell Death to Overcome Drug Resistance with Multitargeting Bis-Naphthalimides as Potent Antibacterial Agents against Enterococcus Faecalis, *J. Mater. Chem. B*, 2024, **12**(23), 5645–5660.

 This journal is © The Royal Society of Chemistry 2026